

Ultra-cold fermions in the flatland: evolution from BCS to Bose superfluidity in two-dimensions with spin-orbit and Zeeman fields

Li Han and C. A. R. Sá de Melo

School of Physics, Georgia Institute of Technology, Atlanta, Georgia 30332, USA

(Dated: September 10, 2018)

We discuss the evolution from BCS to Bose superfluidity for ultracold fermions in two-dimensions and in the presence of simultaneous spin-orbit and Zeeman fields. We analyze several thermodynamic properties to characterize different superfluid phases including pressure, compressibility, induced polarization, and spin susceptibility. Furthermore, we compute the momentum distribution and construct topological invariants for each of the superfluid phases.

PACS numbers: 03.75.Ss, 67.85.Lm, 67.85.-d

Ultra-cold Fermi atoms are one of the most interesting physical systems of the last decade, as they have served as quantum simulators of crossover phenomena and phase transitions encountered in several areas of physics. Due to their tunable interactions, atoms like ^6Li and ^{40}K have been used to study the crossover from BCS to BEC superfluidity, to simulate superfluidity in neutron stars, and to investigate unitary interactions which are of great interest in nuclear physics. Furthermore, the ability to control the internal spin state of the atoms by using radio-frequencies (RF) enabled the studies of quantum and classical phase transitions as a function of interactions and population imbalance. These tools have permitted the study of crossover phenomena and phase transitions, and have validated the symmetry based classification of phase transitions put forth by Landau over the thermodynamic classification proposed earlier by Ehrenfest.

Very recently three new tools have been developed for ultra-cold fermions. The first tool is a method that allows for the extraction of thermodynamic properties - such as pressure, entropy, compressibility and spin-susceptibility - for uniform systems by using local density profiles [1, 2]. The second tool provides the ability to trap two dimensional fermions in the quantum degenerate regime [3, 4]. The third tool is the creation of artificial spin-orbit and Zeeman fields [5], which allows for the visitation of previously inaccessible physical regimes, such as the limit of strong spin-orbit coupling (SOC). Thus far, the SOC created is of the equal Rashba-Dresselhaus (ERD) type instead of Rashba-only [6] or Dresselhaus-only [7]. The emergence of the third tool in the context of ultra-cold bosons [5] has generated substantial theoretical interest about the possibility of applying the technique to three-dimensional ultra-cold fermions [8, 9, 11–15, 23]. Several groups studied the Rashba SOC [9, 11–13, 23], which occurs naturally in condensed matter physics, while our group explored the ERD case [14, 15]. In the context of ultra-cold fermions, the combination of the first two new tools has been achieved experimentally very recently [16], and there are recent reports that ERD SOC has been created in fermionic systems of ^{40}K [17] and ^6Li [18].

In this manuscript, we discuss the combination of these

three new techniques to describe the evolution from BCS to Bose superfluidity in two-dimensions, which in the context of ultra-cold fermions has been discussed for population balanced s -wave [19], p -wave [20], and imbalanced s -wave [21] systems without SOC. Preliminary accounts of the effects of Rashba SOC have recently appeared in the cold atom literature [22, 23]. Here, we study the simultaneous effects of ERD spin-orbit and Zeeman fields, which produce a very rich phase diagram consisting of different topological superfluid. To describe these novel phases, we discuss their spectroscopic and thermodynamic properties.

Hamiltonian: We start with the total Hamiltonian $H = H_{\text{sp}} + H_{\text{int}}$, where the single-particle part is ($\hbar = 1$)

$$H_{\text{sp}} = \sum_{\mathbf{k}, s, s', i} \psi_s^\dagger(\mathbf{k}) \left[\hat{K} \delta_{ss'} - h_i(\mathbf{k}) \sigma_{i, ss'} \right] \psi_{s'}(\mathbf{k}). \quad (1)$$

Here, $\hat{K} = k^2/(2m) - \mu$ is the kinetic energy in reference to the chemical potential μ and $h_i(\mathbf{k})$ is the spin-orbit plus Zeeman field along the i -direction ($s, s' = \uparrow, \downarrow$, $i = x, y, z$). In the present case, we consider only the ERD SOC field $\mathbf{h}_{\text{ERD}} = (0, vk_x, 0)$ [5, 14, 15] and Zeeman field $\mathbf{h}_{\text{ZEE}} = (0, h_y, h_z)$. The current Hamiltonian matrix that can be created in the laboratory using Raman beams is of the form $H_{\text{ZSO}} = -h_z \sigma_z - h_y \sigma_y - h_{\text{ERD}} \sigma_y$, where $h_z = (\Omega/2)$ with Ω being the Raman intensity, $h_y = (\delta/2)$ with δ being the detuning, and $h_{\text{ERD}} = vk_x$ with v being a measure of the SOC strength.

The interaction Hamiltonian is

$$H_{\text{int}} = \sum_{\mathbf{k}, \mathbf{k}', \mathbf{q}} V_{\mathbf{k}\mathbf{k}'} b_{\mathbf{q}}^\dagger(\mathbf{k}) b_{\mathbf{q}}(\mathbf{k}'), \quad (2)$$

where $b_{\mathbf{q}}^\dagger(\mathbf{k}) = \psi_{\uparrow}^\dagger(\mathbf{k} + \mathbf{q}/2) \psi_{\downarrow}^\dagger(-\mathbf{k} + \mathbf{q}/2)$ is the creation operator for a pair of fermions with center of mass momentum \mathbf{q} and relative momentum $2\mathbf{k}$. The interaction term $V_{\mathbf{k}\mathbf{k}'}$ is the Fourier transform of the contact interaction $V(\mathbf{r}, \mathbf{r}') = -g \delta(\mathbf{r} - \mathbf{r}')$ ($g > 0$).

The single-particle Hamiltonian H_{sp} can be diagonalized by a momentum dependent $\text{SU}(2)$ transformation into the helicity basis $\Phi^\dagger(\mathbf{k}) = M(\mathbf{k}) \Psi^\dagger(\mathbf{k})$, where the

helicity creation operators $\Phi^\dagger(\mathbf{k}) = (\phi_{\uparrow}^\dagger(\mathbf{k}), \phi_{\downarrow}^\dagger(\mathbf{k}))$ are expressed as linear combinations of the standard creation operators $\Psi^\dagger(\mathbf{k}) = (\psi_{\uparrow}^\dagger(\mathbf{k}), \psi_{\downarrow}^\dagger(\mathbf{k}))$. The eigenvalues of the Hamiltonian matrix $\mathbf{H}_{\text{sp}}(\mathbf{k})$ are $\xi_{\uparrow, \downarrow}(\mathbf{k}) = K(\mathbf{k}) \mp |\mathbf{h}_{\text{eff}}(\mathbf{k})|$, corresponding to the helicity spin \uparrow (\downarrow) being aligned (anti-aligned) with respect to the effective magnetic field $\mathbf{h}_{\text{eff}}(\mathbf{k}) = (0, h_{\text{ERD}}(\mathbf{k}), h_z)$. Here, the magnitude of the effective field is $|\mathbf{h}_{\text{eff}}(\mathbf{k})| = \sqrt{h_z^2 + v^2 k_x^2}$ and $K(\mathbf{k}) = \epsilon_{\mathbf{k}} - \mu = k^2/(2m) - \mu$.

In the helicity basis, the interaction Hamiltonian transforms as $H_{\text{int}} = -g \sum_{\mathbf{q} \alpha \beta \gamma \delta} B_{\alpha \beta}^\dagger(\mathbf{q}) B_{\gamma \delta}(\mathbf{q})$, where $\alpha, \beta, \gamma, \delta = \uparrow, \downarrow$. Pairing is now described by the operator $B_{\alpha \beta}^\dagger(\mathbf{q}) = \sum_{\mathbf{k}} \Lambda_{\alpha \beta}(\mathbf{k}_1, \mathbf{k}_2) \Phi_\alpha^\dagger(\mathbf{k}_1) \Phi_\beta^\dagger(\mathbf{k}_2)$ and its Hermitian conjugate, with momentum indices $\mathbf{k}_1 = \mathbf{k} + \mathbf{q}/2$ and $\mathbf{k}_2 = -\mathbf{k} + \mathbf{q}/2$. Pairing occurs between fermions of momenta \mathbf{k}_1 and \mathbf{k}_2 in two different helicity bands (inter-helicity pairing), as well as within the same helicity band (intra-helicity pairing). The tensor $\Lambda_{\alpha \beta}(\mathbf{k}_1, \mathbf{k}_2)$ contains the matrix elements of the momentum dependent SU(2) rotation into the helicity basis, and reveals that the center of mass momentum $\mathbf{k}_1 + \mathbf{k}_2 = \mathbf{q}$ and the relative momentum $\mathbf{k}_1 - \mathbf{k}_2 = 2\mathbf{k}$ are coupled and no longer independent.

For pairing at $\mathbf{q} = 0$, the order parameter for superfluidity is the tensor $\Delta_{\alpha \beta}(\mathbf{k}) = \Delta_0 \Lambda_{\alpha \beta}(\mathbf{k}, -\mathbf{k})$, where $\Delta_0 = -g \sum_{\gamma \delta} \langle B_{\gamma \delta}(\mathbf{0}) \rangle$, leading to components: $\Delta_{\uparrow \uparrow}(\mathbf{k}) = i \tilde{\Delta}_T(\mathbf{k})$ for helicity projection $\lambda = +1$; $\Delta_{\uparrow \downarrow}(\mathbf{k}) = -\Delta_{\downarrow \uparrow}(\mathbf{k}) = -\tilde{\Delta}_S(\mathbf{k})$ for helicity projection $\lambda = 0$; and $\Delta_{\downarrow \downarrow}(\mathbf{k}) = -i \tilde{\Delta}_T(\mathbf{k})$ for helicity projection $\lambda = -1$. The amplitudes $\tilde{\Delta}_T(\mathbf{k}) = \Delta_0 h_{\text{ERD}}(\mathbf{k})/|\mathbf{h}_{\text{eff}}(\mathbf{k})|$ and $\tilde{\Delta}_S(\mathbf{k}) = \Delta_0 h_z/|\mathbf{h}_{\text{eff}}(\mathbf{k})|$ reflect the triplet and singlet components of the order parameter in the helicity basis. For the ERD case, $\tilde{\Delta}_T(\mathbf{k})$ is odd and $\tilde{\Delta}_S(\mathbf{k})$ is even under parity \mathcal{P} in momentum space, while they are both invariant under time reversal \mathcal{T} , and both reflect the broken U(1) symmetry of the superfluid phase. The triplet and singlet sectors in the helicity basis are not independent as the interactions from which they originate occur only in the singlet s -wave of the original spin basis, and the relation $|\tilde{\Delta}_T(\mathbf{k})|^2 + |\tilde{\Delta}_S(\mathbf{k})|^2 = |\Delta_0|^2$ holds.

It is worth emphasizing that in the triplet sector $\Delta_{\uparrow \uparrow}(\mathbf{k})$ and $\Delta_{\downarrow \downarrow}(\mathbf{k})$ contain not only p -wave, but also f -wave and higher odd partial waves in two dimensions, as can be seen from a *multipole* expansion of $|\mathbf{h}_{\text{eff}}(\mathbf{k})|^{-1} = [h_z^2 + h_{\text{ERD}}^2(\mathbf{k})]^{-1/2}$ for finite h_z . Similarly in the singlet sector $\Delta_{\uparrow \downarrow}(\mathbf{k})$ and $\Delta_{\downarrow \uparrow}(\mathbf{k})$ contain s -wave, d -wave and higher even partial waves, as long as the Zeeman field h_z is non-zero. Higher angular momentum pairing occurs because the local (zero-ranged) interaction in the (\uparrow, \downarrow) spin basis is transformed into a finite-ranged anisotropic interaction in the helicity basis (\uparrow, \downarrow) .

The effective Hamiltonian in the helicity basis takes

the matrix form

$$H_{\text{eff}}(\mathbf{k}) = \begin{pmatrix} \xi_{\uparrow}(\mathbf{k}) & 0 & \Delta_{\uparrow \uparrow}(\mathbf{k}) & \Delta_{\uparrow \downarrow}(\mathbf{k}) \\ 0 & \xi_{\downarrow}(\mathbf{k}) & \Delta_{\downarrow \uparrow}(\mathbf{k}) & \Delta_{\downarrow \downarrow}(\mathbf{k}) \\ \Delta_{\uparrow \uparrow}^*(\mathbf{k}) & \Delta_{\uparrow \downarrow}^*(\mathbf{k}) & -\xi_{\uparrow}(\mathbf{k}) & 0 \\ \Delta_{\uparrow \downarrow}^*(\mathbf{k}) & \Delta_{\downarrow \downarrow}^*(\mathbf{k}) & 0 & -\xi_{\downarrow}(\mathbf{k}) \end{pmatrix}. \quad (3)$$

The eigenvalues for the quasiparticle bands are

$$E_{p\pm}(\mathbf{k}) = \sqrt{(E_S(\mathbf{k}) \pm |\mathbf{h}_{\text{eff}}(\mathbf{k})|)^2 + |\Delta_T(\mathbf{k})|^2}, \quad (4)$$

where $E_S(\mathbf{k}) = \sqrt{|K(\mathbf{k})|^2 + |\tilde{\Delta}_S(\mathbf{k})|^2}$ is a characteristic energy for the singlet sector. The eigenvalues for quasihole bands are $E_{h\pm}(\mathbf{k}) = -E_{p\pm}(\mathbf{k})$. The effective field $|\mathbf{h}_{\text{eff}}(\mathbf{k})|$ emerges from the energy difference between the helicity energies $|\mathbf{h}_{\text{eff}}(\mathbf{k})| = [\xi_{\downarrow}(\mathbf{k}) - \xi_{\uparrow}(\mathbf{k})]/2$, while $K(\mathbf{k}) = [\xi_{\downarrow}(\mathbf{k}) + \xi_{\uparrow}(\mathbf{k})]/2$ is the average energy of the helicity bands.

Only $E_{p-}(\mathbf{k})$ has zeros or nodes, provided that the following conditions are satisfied simultaneously: first, the effective magnetic field energy must equal to the *excitation energy* for the singlet sector $|\mathbf{h}_{\text{eff}}(\mathbf{k})| = E_S(\mathbf{k})$; second, the triplet component of the order parameter must vanish $|\tilde{\Delta}_T(\mathbf{k})| = 0$. The nodal structure for $E_{p-}(\mathbf{k})$ dominates the physics at low energies. For the ERD case, $|h_{\text{ERD}}(\mathbf{k})| = v|k_x|$. Therefore, zeros of $E_{p-}(\mathbf{k})$ must occur when $k_x = 0$, which gives rise to up to four possible point nodes that are determined by the real solutions of k_y to the equation $(k_y^2/(2m) - \mu)^2 + |\Delta_0|^2 = h_z^2$.

To obtain the phase diagram, we calculate the thermodynamic potential $\Omega = -T \ln [\text{Tr} e^{-H_{\text{eff}}/T}]$, and solve self-consistently the order parameter equation $\partial \Omega / \partial |\Delta_0|^2 = 0$ and the number equation $N = -(\partial \Omega / \partial \mu)_{T, V}$. The contact interaction g/V is expressed in terms of the two-body binding energy E_b in the absence of SOC via the relation $V/g = \sum_{\mathbf{k}} 1/(2\epsilon_{\mathbf{k}} + E_b)$.

In Fig. 1, we show the zero temperature phase diagrams of Zeeman field h_z versus the two-body binding energy E_b as well as induced population imbalance P_{ind} versus binding energy for both vanishing and large finite SOC ($v/v_F = 0$ and 0.8). We label the uniform superfluid phases with zero, one or two pairs of nodes as US-0, US-1, and US-2, respectively. The US-2/US-1 phase boundary is determined by the condition $\mu = \sqrt{h_z^2 - |\Delta_0|^2}$, when $|h_z| > |\Delta_0|$; the US-0/US-2 boundary is determined by the Clogston-like condition $|h_z| = |\Delta_0|$ when $\mu > 0$, where the gapped US-0 phase disappears leading to the gapless US-2 phase; and the US-0/US-1 phase boundary is determined by $\mu = -\sqrt{h_z^2 - |\Delta_0|^2}$, when $|h_z| > |\Delta_0|$. Furthermore, within the US-0 phase, a crossover line between an indirectly gapped and a directly gapped US-0 phase occurs at $\mu = 0$. Non-uniform (NU) phases also emerge in regions where uniform phases are thermodynamically unstable for $v/v_F \neq 0$, however NU phases only exist in the regime of $0 < v/v_F < (v/v_F)_c$, where $(v/v_F)_c \approx 0.6$. Possible NU phases include phase separation, modulated superfluids or supersolid. These possible

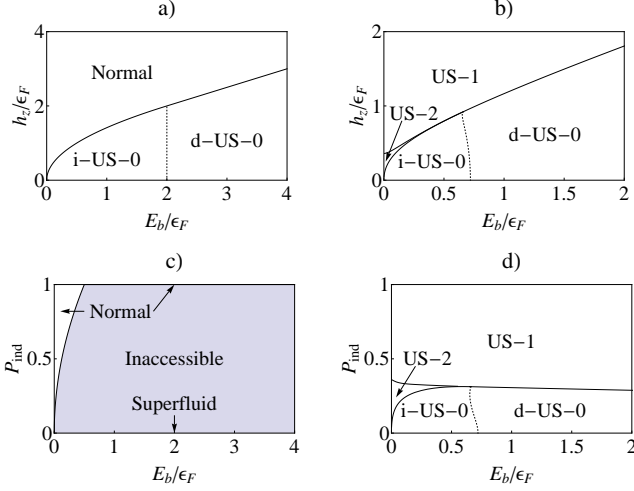


FIG. 1: Zero temperature ($T = 0$) phase diagrams of Zeeman field h_z/ϵ_F versus two-body binding energy E_b/ϵ_F for equal Rashba-Dresselhaus (ERD) SOC (a) $v/v_F = 0$ and (c) $v/v_F = 0.8$. The corresponding phase diagrams for the induced population imbalance P_{ind} versus E_b/ϵ_F are shown in (b) $v/v_F = 0$ and (d) $v/v_F = 0.8$. Here, $\epsilon_F = k_F^2/(2m)$ and $v_F = k_F/m$ are the Fermi energy and momentum respectively, and k_F is related to the particle density n via $k_F = (3\pi^2 n)^{1/3}$.

phases are not illustrated in Fig. 1 since we are interested in comparisons between the zero SOC case $v/v_F = 0$ and the large SOC case $v/v_F > (v/v_F)_c$. In the latter case, a tri-critical point occurs at the intersection of the US-0, US-1, and US-2 (where $\mu = 0$ and $|h_z| = |\Delta_0|$).

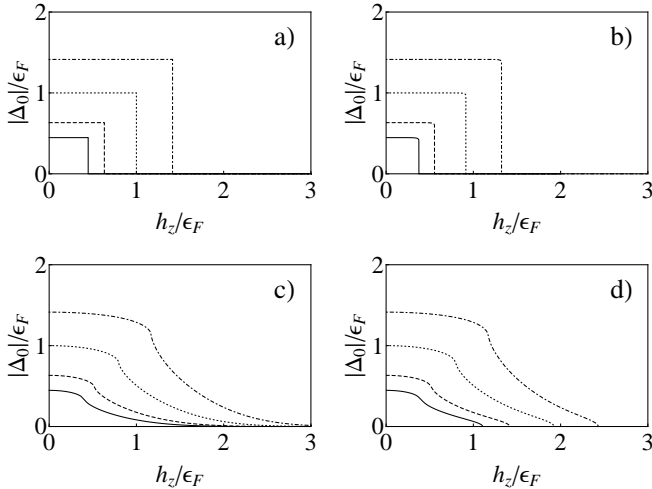


FIG. 2: The order parameter amplitude $|\Delta_0|/\epsilon_F$ as a function of external Zeeman field h_z/ϵ_F for (a) $v/v_F = 0$, $T/\epsilon_F = 0$, (b) $v/v_F = 0$, $T/\epsilon_F = 0.03$, (c) $v/v_F = 0.8$, $T/\epsilon_F = 0$, (d) $v/v_F = 0.8$, $T/\epsilon_F = 0.03$ at various binding energies $E_b/\epsilon_F = 0.1$ (solid line), $E_b/\epsilon_F = 0.2$ (dashed line), $E_b/\epsilon_F = 0.5$ (dotted line), $E_b/\epsilon_F = 1.0$ (dot-dashed line).

It is important to note from the phase diagrams that for finite SOC ($v/v_F > 0$) it is always possible to form

pairs in the lower helicity band $\xi_{\uparrow}(\mathbf{k})$ no matter how large the Zeeman field h_z is. This is because an induced triplet component of the order parameter emerges and circumvents the standard pair breaking Clogston limit for singlet pairing. Thus, the stable superfluid phase for large h_z at $T = 0$ is the US-1 phase as shown in Fig. 1 provided that $v/v_F \neq 0$. This is clearly seen in Fig. 2 where the order parameter is shown for the cases of $v/v_F = 0$ and $v/v_F = 0.8$. In the first case ($v/v_F = 0$), the Clogston limit at $T = 0$ occurs when $h_z/\epsilon_F \sim |\Delta_0|/\epsilon_F$ as seen in Fig. 2a, where the order parameter jumps discontinuously to zero at a critical value of $(h_z/\epsilon_F)_c$. The discontinuity occurs also at finite temperatures (Fig. 2b), rendering the transition from the superfluid to the normal phase discontinuous according to Landau's classification or first order according to Ehrenfest's. For $v/v_F = 0.8$, the absence of the Clogston paramagnetic limit at zero temperature is clearly seen in Fig. 2c, where the order parameter vanishes only asymptotically as $h_z/\epsilon_F \rightarrow \infty$ because of the induced triplet component in the helicity basis. As the temperature is raised, thermal fluctuations break pairs, the order parameter vanishes, and the normal state is reached beyond a critical Zeeman field $(h_z/\epsilon_F)_c$, which is an increasing function of the binding energy E_b/ϵ_F for fixed $v/v_F > (v/v_F)_c$. This also occurs for Rashba-only couplings in two-dimensions [22], and for ERD couplings in three-dimensions [15].

These superfluid phases can be classified according to the topological properties of their low-energy excitation spectrum $E_{p-}(\mathbf{k})$. The nodes of $E_{p-}(\mathbf{k})$ can be viewed as vortex singularities in momentum space. Consider the two-dimensional unit vector $\hat{\mathbf{m}}(\mathbf{k}) = (m_x, m_y)$, where $m_x(\mathbf{k}) = [E_S(\mathbf{k}) - |\mathbf{h}_{\text{eff}}(\mathbf{k})|]/E_{p-}(\mathbf{k})$ and $m_y(\mathbf{k}) = \tilde{\Delta}_T(\mathbf{k})/E_{p-}(\mathbf{k})$. The topological charge is the winding (Chern) number $N_w = (2\pi)^{-1} \oint d\ell \hat{\mathbf{z}} \cdot \hat{\mathbf{m}} \times d\hat{\mathbf{m}}/d\ell$, where the line integral is over any line in the k_x - k_y plane enclosing a zero of $E_{p-}(\mathbf{k})$. The topological charges take values ± 1 . In the US-2 (US-1) phase the topological charges follow the sequence $+-+-$ ($+-$) for the four (two) nodal points as we scan k_y from negative to positive.

The change in nodal structure is associated with bulk topological transitions of the Lifshitz class as noted for p -wave [20, 24] and d -wave [25, 26] superfluids. The loss of nodal regions of $E_{p-}(\mathbf{k})$ correspond to annihilation of Dirac quasi-particles with opposite momenta and opposite topological charge (US-1/US-2 and US-1/d-US-0), or with the same momenta but opposite topological charge (US-2/i-US-0). For instance, starting from the US-1 (US-2) phase, Dirac quasi-particles annihilate at zero momentum producing bulk Majorana quasi-particles at the US-1/d-US-0 (US-2/US-1) phase boundary, which then become massive Dirac fermions near zero momentum with positive mass (negative mass) in the d-US-0 (US-1) phase. However, zero-momentum bulk Majorana quasi-particles do not occur at the US-2/i-US-0 phase boundary, as the four node superfluid US-2 leads be-

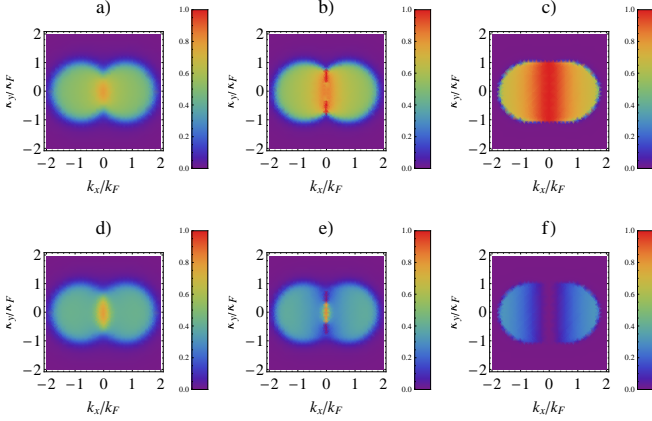


FIG. 3: (color online) The momentum distributions $n_s(k_x, k_y)$ for ERD SOC $v/v_F = 0.8$ and $E_b/\epsilon_F = 0.1$ at $T = 0$, where $s = \uparrow (\downarrow)$ for upper (lower) panels. (a)(d) i-US-0 phase with $h_z/\epsilon_F = 0.2$; (b)(e) US-2 phase with $h_z/\epsilon_F = 0.4$; (c)(f) US-1 phase with $h_z/\epsilon_F = 1.0$. The color coding varies continuously from purple ($n_s = 0$) to red ($n_s = 1$).

comes a doubly-degenerate two-node superfluid at finite momentum at the phase boundary and then becomes an indirect gap superfluid.

The emergence of Dirac fermions produces dramatic changes in momentum distributions [25]

$$n_{\mathbf{k},s} = \frac{1}{2} \left[1 - \sum_j n_F[E_j(\mathbf{k})] \frac{\partial E_j(\mathbf{k})}{\partial \mu_s} \right], \quad (5)$$

which are illustrated in Fig. 3 for parameters $v/v_F = 0.8$ and $E_b/\epsilon_F = 0.1$ at $T = 0$. Different topological phases are shown for different values of Zeeman field h_z . Here, $n_F[E_j(\mathbf{k})] = 1/(\exp[E_j(\mathbf{k})/T] + 1)$ is the Fermi function. For the i-US-0 phase the momentum distributions are smooth functions of $\mathbf{k} = (k_x, k_y)$ until the i-US-0/US-2 phase boundary is reached where doubly degenerate nodes emerge at $\mathbf{k} = (0, \pm\sqrt{2m\mu})$. Beyond this point discontinuities develop in $n_{\mathbf{k},s}$, which is due to the finite Zeeman field and can be best seen in its \uparrow component. Within the US-2 phase there are four discontinuities at the zeros of $E_{p-}(\mathbf{k})$, which are located at $\mathbf{k} = \left(0, \pm\sqrt{2m\left[\mu \pm \sqrt{h_z^2 - |\Delta_0|^2}\right]}\right)$. Around these zeros the energy has cusps and the dispersion is linear. As h_z is increased further, the US-2/US-1 boundary is crossed and the inner Dirac fermions annihilate, leaving discontinuities in the momentum distribution occur only at two nodes $\mathbf{k} = \left(0, \pm\sqrt{2m\left[\mu + \sqrt{h_z^2 - |\Delta_0|^2}\right]}\right)$. The final US-1 phase is highly polarized as can be seen from the great contrast between Fig. 3c and 3f.

We show in Fig. 4 several thermodynamic properties as a function of Zeeman field h_z/ϵ_F for different binding energies at $T = 0$. In Fig. 4a, we show the pressure $P =$

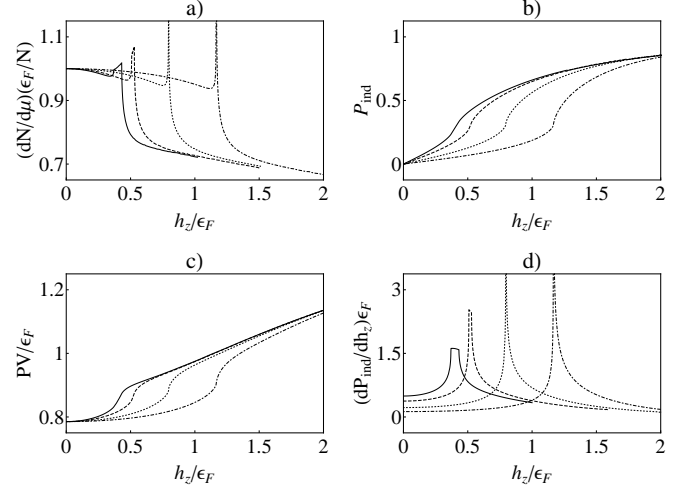


FIG. 4: Various thermodynamic quantities versus Zeeman field h_z/ϵ_F for different values of binding energies $E_b/\epsilon_F = 0.1$ (solid line), $E_b/\epsilon_F = 0.2$ (dashed line), $E_b/\epsilon_F = 0.5$ (dotted line), and $E_b/\epsilon_F = 1.0$ (dot-dashed line). (a) The pressure P ; (b) The isothermal compressibility $N^2 \kappa_T$; (c) The induced polarization P_{ind} ; (d) The spin susceptibility χ_{zz} .

$-\Omega/V$. In Fig. 4b, we show the isothermal compressibility $\kappa_T = -V^{-1}(\partial V/\partial P)_T$, which can also be written as $\kappa_T = N^{-2}(\partial N/\partial \mu)_T$. In Fig. 4c and 4d, we show the induced polarization $P_{\text{ind}} = (N_{\uparrow} - N_{\downarrow}) / (N_{\uparrow} + N_{\downarrow})$, and the spin susceptibility $\chi_{zz} = (\partial P_{\text{ind}}/\partial h_z)_{T,V}$. According to Fig. 1b, if we fix the value of E_b and increase the Zeeman field h_z from zero, we may cross several phase boundaries, e.g., from i-US-0 to US-2 to US-1, or from d-US-0 to US-1. Correspondingly, both κ_T and χ_{zz} are non-analytic at the phase boundaries (Fig. 4c and 4d), thus providing clear thermodynamic signatures of the topological quantum phase transitions described above.

In summary, we investigated the effects of Zeeman fields and ERD SOC on the superfluidity of two-dimensional ultra-cold fermions from the BCS to the Bose regime. We constructed the ground-state phase diagram of Zeeman field versus spin-orbit coupling, identified bulk topological (Lifshitz) phase transitions between gapped and gapless superfluid. We also described the existence of a tri-critical point in the strong spin-orbit coupling regime. Lastly, we analyzed the excitation spectrum and the momentum distribution, as well as thermodynamic quantities including the pressure, compressibility, induced polarization, and spin-susceptibility, all of which provide signatures of the phase transitions.

We thank Wei Zhang for discussions and ARO (W911NF-09-1-0220) for support.

-
- [1] N. Navon et al., Science **328**, 729 (2010).
 - [2] M. Ku et al., Science **335**, 563 (2012).

- [3] K. Martiyanov, V. Makhlov, and A. Turlapov, Phys. Rev. Lett. **105**, 030404 (2010).
- [4] M. Feld et al., Nature **480**, 75 (2011).
- [5] Y. J. Lin, K. Jimenez-Garcia, and I. B. Spielman, Nature **471**, 83 (2011).
- [6] Y. A. Bychkov and E. I. Rashba, J. Phys. C **17**, 6029 (1984).
- [7] G. Dresselhaus, Phys. Rev. **100**, 580 (1955).
- [8] M. Chapman and C. Sá de Melo, Nature **471**, 41 (2011).
- [9] J. P. Vyasankere, S. Zhang, and V. B. Shenoy, Phys. Rev. B **84**, 014512 (2011).
- [10] M. Gong, S. Tewari, and C. Zhang, Phys. Rev. Lett. **107**, 195303 (2011).
- [11] H. Hu, L. Jiang, X. J. Jiu, and H. Pu, Phys. Rev. Lett. **107**, 195304 (2011).
- [12] Z.-Q. Yu and H. Zhai, Phys. Rev. Lett. **107**, 195305 (2011).
- [13] M. Iskin and A. L. Subasi, Phys. Rev. Lett. **107**, 050402 (2011).
- [14] L. Han, C. A. R. Sá de Melo, Phys. Rev. A **85**, 011606(R) (2012).
- [15] K. Seo, L. Han, and C. A. R. Sá de Melo, Phys. Rev. A **85**, 033601 (2012).
- [16] A. T. Sommer et al., Phys. Rev. Lett. **108**, 045302 (2012).
- [17] P. Wang et al., arXiv:1204.1887v1 (2012).
- [18] L. W. Cheuk et al., arXiv:1205.3483 (2012).
- [19] S. S. Botelho and C. A. R. Sá de Melo, Phys. Rev. Lett. **96**, 040404 (2006).
- [20] S. S. Botelho and C. A. R. Sá de Melo, J. Low. Temp. Phys. **140**, 409 (2005).
- [21] J. Tempere, S. N. Klimin, and J. T. Devreese, Phys. Rev. A **79**, 053637 (2009).
- [22] J. Zhou, W. Zhang, and W. Yi, Phys. Rev. A **84**, 063603 (2011).
- [23] G. Chen, M. Gong, and C. Zhang, Phys. Rev. A **85**, 013601 (2011).
- [24] G. E. Volovik, *Exotic Properties of Superfluid ^3He* , World Scientific, Singapore (1992).
- [25] R. D. Duncan and C. A. R. Sá de Melo, Phys. Rev. B **62**, 9675 (2000).
- [26] S. S. Botelho and C. A. R. Sá de Melo, Phys. Rev. B **71**, 134507 (2005).
- [27] M. Nakahara, *Geometry, Topology and Physics*, Adam Hilger, Bristol (1990).